



# Multivariate metal-organic frameworks enable chemical shift-encoded MRI with femtomolar sensitivity for biological systems

Received: 9 January 2025

Accepted: 11 July 2025

Published online: 24 July 2025



Qingbin Zeng<sup>1,2,5</sup>, Quer Yue<sup>1,2,5</sup>, Ming Zhang<sup>1,2</sup>, Rui Zhou<sup>1,2</sup>, Zhen Wang<sup>1,2</sup>, Zhongyu Xiao<sup>1,2</sup>, Yaping Yuan<sup>1,2</sup>, Xiuchao Zhao<sup>1,2</sup>, Weiping Jiang<sup>1,2</sup>, Lei Zhang<sup>1,2</sup>, Yuqi Yang<sup>1,2</sup>, Minghui Yang<sup>1,2</sup>, Haidong Li<sup>1,2</sup>, Louis-S. Bouchard<sup>3</sup>, Qianni Guo<sup>1,2</sup>✉ & Xin Zhou<sup>1,2,4</sup>✉

Fluorescent molecules with specific target moieties are essential for histopathological analysis, but their limited tissue penetration depth makes *in vivo*, *in situ* color encoding analysis challenging. Magnetic resonance imaging (MRI) offers deep tissue penetration. When combined with chemical shift-encoded MRI reporters, it enables *in vivo* chemical shift encoding for biotarget imaging and analysis. These reporters require both strong signal intensity and large chemical shift window. However, conventional proton MRI reporters, with low sensitivity and a small chemical shift window, limit their *in vivo* applications. Here, we describe a chemical shift-encoded hyperpolarized <sup>129</sup>Xe MRI reporter based on the multivariate metal-organic framework, NiZn-ZIF-8, to overcome these challenges. The proposed NiZn-ZIF-8 gives distinct chemical shifts for dissolved and entrapped <sup>129</sup>Xe without signal interference, enhancing the <sup>129</sup>Xe NMR signal by 210 times compared to dissolved <sup>129</sup>Xe in water and biological media. This enables detection threshold at  $\approx 4$  fM concentrations, setting a record for the lowest concentration of xenon hosts detected in nanomaterials. Additionally, NiZn-ZIF-8 exhibits good *in vivo* MRI performance, allowing xenon encoding and distinction in rat lungs. NiZn-ZIF-8 represents a versatile and powerful platform for advanced molecular imaging and *in vivo* biomedical diagnostics.

Fluorescence imaging offers numerous advantages, such as high sensitivity and real-time imaging, making it an invaluable tool for studying molecular mechanisms and early disease diagnosis<sup>1,2</sup>. Many fluorescent molecules have been developed, which can color-encode different targets for histopathological analysis and cellular imaging based on their emission wavelengths after being labeled with specific targeting

moieties. However, challenges remain in *in vivo* color-encoded imaging, including background interference, fluorescence signal decay, and limited tissue penetration depth.

Magnetic resonance imaging (MRI) is a modality in clinical diagnostics and biomedical research that allows for the non-invasive visualization of internal structures and biological processes without

<sup>1</sup>State Key Laboratory of Magnetic Resonance Spectroscopy and Imaging, National Center for Magnetic Resonance in Wuhan, Wuhan Institute of Physics and Mathematics, Innovation Academy for Precision Measurement Science and Technology, Chinese Academy of Sciences Wuhan 430071, P. R. China. <sup>2</sup>University of Chinese Academy of Sciences, Beijing 100049, P. R. China. <sup>3</sup>UCLA Department of Chemistry and Biochemistry, The Molecular Biology Institute, Jonsson Comprehensive Cancer Center, California NanoSystems Institute, University of California, Los Angeles 90095, USA. <sup>4</sup>School of Biomedical Engineering, Hainan University, Haikou 570228, P. R. China. <sup>5</sup>These authors contributed equally: Qingbin Zeng, Quer Yue. ✉e-mail: [qian-niguo@wipm.ac.cn](mailto:qian-niguo@wipm.ac.cn); [xinzhou@wipm.ac.cn](mailto:xinzhou@wipm.ac.cn)

limitations in tissue penetration depth. Chemical shift is one of the most important parameters in nuclear magnetic resonance (NMR), closely related to the chemical environment of the atomic nucleus. It plays a crucial role in substance identification and molecular structure analysis. Different substances can be encoded by their chemical shifts for analysis. When combined with functionalized chemical shift-encoded MRI reporters, it enables *in vivo* chemical shift-encoded imaging for biotargets. To achieve effective chemical shift-encoded MRI, the reporters must provide both strong signal intensity and a large chemical shift window. However, conventional proton chemical shift-encoded MRI reporters suffer from fundamental limitations, such as low sensitivity and a small chemical shift window, which limit their application in complex biological systems.

Because of the associated high sensitivity, large chemical shift window, and absence of biological background signals, hyperpolarized  $^{129}\text{Xe}$  gas, produced by the spin-exchange optical pumping (SEOP) method, has established itself as a promising agent<sup>3–9</sup>. Dissolution of this gas in aqueous media or in blood results in a single peak at  $\approx 193$  ppm, far off from the gaseous  $^{129}\text{Xe}$  signal in  $\approx 0$  ppm. Trapping xenon atoms with molecular cages, such as cryptophanes and cucurbit[6]uril, generates a distinct NMR signal for entrapped xenon, which differs from that of dissolved xenon and xenon gas, allowing for encoding by chemical shift for analysis. These chemical shift-encoded molecular cages, similar to fluorescent molecules, can be functionalized with various target moieties, enabling the detection of different biomolecules or cells<sup>10–14</sup>. However, these molecular cages typically exhibit weak  $^{129}\text{Xe}$  NMR signals, particularly in aqueous and biological environments, due to low xenon loading and signal intensity. Most of such drawbacks hampered their practical applications in molecular imaging, much more so *in vivo* experiments, where the signal is required to be strong and stable, and specificity often becomes an issue. So far, enhancement efforts toward  $^{129}\text{Xe}$  NMR signals through physical and chemical modifications have been minor<sup>15,16</sup>; thus, there is an urgent need for the strategy of amplifying  $^{129}\text{Xe}$  signal intensity with its biocompatibility preserved.

Metal-organic frameworks (MOFs) offer a versatile platform to address these challenges. MOFs are crystalline materials that consist of metal clusters or ions bridged by organic ligands, forming highly ordered, porous networks with tunable pore sizes, high surface areas, and robust chemical stability. Such characteristics make MOFs attractive for applications involving gas storage, separation, and sensing<sup>17–23</sup>. Among them, multivariate MOFs (MTV-MOFs) are of particular interest because they integrate multiple building blocks into a single lattice without changing their topology. This MTV methodology allows for fine-tuning of the MOF's internal environment<sup>24–26</sup>, resulting in significantly higher affinities for guest molecules, enhanced signal intensities, and improved selectivity compared to single-component MOFs<sup>27–31</sup>. In this paper, we introduce a multivariate MOF, NiZn-ZIF-8, purposefully engineered to enhance the entrapped  $^{129}\text{Xe}$  NMR signal intensity, to develop a chemical shift-encoded reporter for hyperpolarized  $^{129}\text{Xe}$  MRI *in vivo*. Incorporation of nickel into the ZIF-8 framework provides some subtle adjustments of its pore environment in such a way that hyperpolarized xenon entrapment and enhanced signal amplification can take place. NiZn-ZIF-8 overcomes critical limitations of traditional xenon-based MRI reporters with fM sensitivity and stability in aqueous and biological media. This work introduces a versatile platform for advanced  $^{129}\text{Xe}$  molecular imaging, with far-reaching possibilities toward transformative *in vivo* applications, and extends the utility of MOFs in biomedical diagnostics.

Previous studies have shown that zeolites and MOFs can adsorb xenon atoms<sup>32–36</sup>. Especially, MOFs such as ZIF-8, IRMOF-1, IRMOF-8, and IRMOF-10 have a strong affinity for xenon atoms, making them effective hosts for hyperpolarized  $^{129}\text{Xe}$  MRI probes<sup>37,38</sup>. Among these, ZIF-8 stands out because of its high surface area and porosity, which

allow it to trap xenon atoms efficiently<sup>37</sup>. Unlike traditional hosts like cryptophanes and cucurbit[6]uril<sup>39,40</sup>, ZIF-8 can effectively concentrate xenon within its porous structure while keeping it separate from the surrounding aqueous phase. This confinement creates a distinct chemical shift in  $^{129}\text{Xe}$  NMR signals, providing a reliable platform for enhancing signal strength.

Building on ZIF-8's natural advantages and the flexibility of MTV-MOFs, we developed NiZn-ZIF-8, to amplify  $^{129}\text{Xe}$  NMR signals in aqueous environments. By incorporating nickel into the ZIF-8 structure, we created a chemical shift-encoded reporter that not only boosts the intensity of the  $^{129}\text{Xe}$  signal but also distinguishes between dissolved and entrapped xenon through distinct chemical shifts.

To implement this strategy, we synthesized a series of nickel-substituted multivariate ZIF-8 materials, called NiZn-ZIF-8, carefully fine-tuning the nickel content to optimize the  $^{129}\text{Xe}$  NMR signal (Fig. 1a, b). The optimized NiZn-ZIF-8 showed a 33% increase in the entrapped  $^{129}\text{Xe}$  NMR signal intensity compared to standard ZIF-8, along with an impressive 210-fold enhancement over dissolved  $^{129}\text{Xe}$  in water and biological media under the same conditions. Additionally, NiZn-ZIF-8 achieves a detection threshold as low as  $\approx 4$  fM. Acting as a highly sensitive, chemical shift-encoded reporter for hyperpolarized  $^{129}\text{Xe}$  MRI, NiZn-ZIF-8 demonstrates good *in vivo* MRI performance. The entrapped xenon can be clearly imaged and distinguished from both dissolved xenon and xenon gas in rat lungs. Its properties—such as good dispersibility in water, a hydrophobic pore environment, pore sizes that closely match xenon atoms, and high stability in aqueous media—make it an ideal platform for concentrating xenon and enhancing signal strength. By addressing key challenges in sensitivity and signal limitations, NiZn-ZIF-8 marks an advancement in molecular imaging technologies, opening possibilities for biomedical applications.

## Results

### Preparation and characterization of MOF samples

A series of NiZn-ZIF-8 nanoparticles were synthesized by adjusting the molar ratio of nickel to zinc salts in a methanol solution containing 2-methylimidazole. The final nickel content in the nanoparticles increased as the initial nickel-to-zinc ratio increased (Supplementary Fig. 1, Supplementary Table 1), and all of these samples exhibited a positive Zeta potential (Supplementary Table 2).

Scanning electron microscopy (SEM) showed that incorporating nickel influenced both the size and shape of the particles. At lower nickel levels (below 0.13%), the nanoparticles maintained a uniform size, while higher nickel content ( $\geq 0.33\%$ ) resulted in more irregular particle shapes (Fig. 2b, Supplementary Figs. 2–8). Despite this, all NiZn-ZIF-8 nanoparticles retained their characteristic dodecahedral shape, as confirmed through SEM and transmission electron microscopy (TEM) (Fig. 2b, c, Supplementary Figs. 2–17).

Elemental mapping revealed that nickel and zinc atoms were evenly distributed throughout individual NiZn-ZIF-8 crystals (Fig. 2d, Supplementary Figs. 18–26). For comparison, we also synthesized and characterized  $\text{Cu}^{2+}$ - and  $\text{Co}^{2+}$ -doped ZIF-8 materials (CuZn-ZIF-8 and CoZn-ZIF-8), which exhibited similar dodecahedral shapes (Supplementary Figs. 27–30). Thermogravimetric analysis (TGA) demonstrated the thermal stability of all MOFs, with no significant weight loss observed below 400 °C (Supplementary Fig. 31).

Nitrogen adsorption measurements at 77 K confirmed the permanent porosity of these materials (Supplementary Figs. 32–56). Notably, NiZn-ZIF-8 showed an increased BET surface area of  $\approx 2000$  m<sup>2</sup> g<sup>-1</sup>, surpassing that of pristine ZIF-8. In contrast, CuZn-ZIF-8 and CoZn-ZIF-8 maintained surface area values similar to pristine ZIF-8 (Supplementary Table 3). Pore size analysis using the nonlocal density functional theory (NLDFT) model revealed an average pore size of about 11 Å for NiZn-ZIF-8, which is consistent with that of pristine ZIF-8 (Supplementary Table 4).

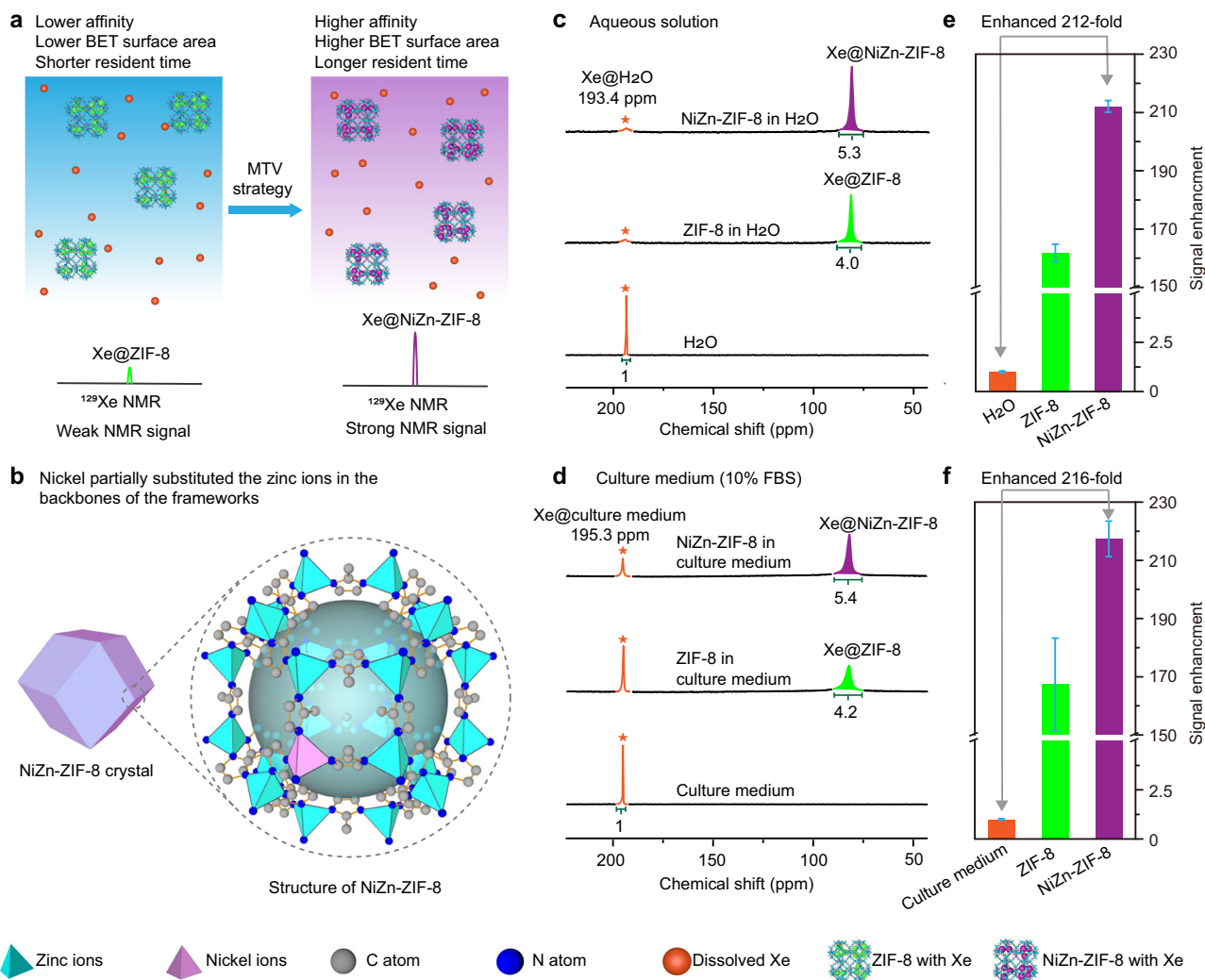


**Fig. 1 | Enhancement of hyperpolarized  $^{129}\text{Xe}$  NMR signal by NiZn-ZIF-8 in aqueous and biological media.** **a** Schematic illustration showing the increase in hyperpolarized  $^{129}\text{Xe}$  NMR signal intensity upon addition of NiZn-ZIF-8 to water. **b** Structural representation of NiZn-ZIF-8, highlighting nickel substitution within the ZIF-8 framework. **c** Hyperpolarized  $^{129}\text{Xe}$  NMR spectra of NiZn-ZIF-8 (25 mg mL $^{-1}$ ), pristine ZIF-8 (25 mg mL $^{-1}$ ), and pure water, demonstrating a significant signal enhancement for NiZn-ZIF-8. **d** Hyperpolarized  $^{129}\text{Xe}$  NMR spectra of NiZn-ZIF-8 (25 mg mL $^{-1}$ ), pristine ZIF-8 (25 mg mL $^{-1}$ ), and culture medium (containing 10% FBS),

showing signal enhancement in a biologically relevant environment. **e** Quantified  $^{129}\text{Xe}$  NMR signal enhancement fold from (c), showing a > 210-fold enhancement for NiZn-ZIF-8 compared to pure water ( $n = 3$  independent experimental replicates). **f** Quantified  $^{129}\text{Xe}$  NMR signal enhancement fold from (d), confirming similar signal enhancements in biological media ( $n = 3$  independent experimental replicates). All NMR spectra were acquired using a zg pulse sequence (rectangular pulse,  $p_1 = 31.8 \mu\text{s}$ ), with a single scan (NS = 1) and line broadening (LB = 10 Hz). Data in (e, f) were presented as mean values  $\pm$  SD. Source data are provided as a Source Data file.

Powder X-ray diffraction (PXRD) analysis confirmed that NiZn-ZIF-8 retained its crystalline integrity and phase purity, showing patterns identical to those of pristine ZIF-8 without any additional peaks (Supplementary Figs. 57–59). This indicates that incorporating Ni $^{2+}$ , Cu $^{2+}$ , or Co $^{2+}$  does not disrupt the original ZIF-8 lattice structure. Further validation through single-crystal X-ray diffraction revealed the partial substitution of Zn $^{2+}$  with Ni $^{2+}$  in the framework backbone (Supplementary Table 5). The stability of NiZn-ZIF-8 was thoroughly tested. Its PXRD pattern remained unchanged even after being immersed in water for one week, demonstrating high stability in aqueous environments (Supplementary Fig. 60).

Further evidence of nickel incorporation was provided by diffuse reflectance visible spectroscopy, which showed two characteristic absorption peaks at 580 nm and 790 nm, corresponding to the [NiN $_4$ ] clusters (Supplementary Fig. 61). These findings align with previous studies $^{41}$ , confirming the stable integration of nickel into the MOF framework.

NiZn-ZIF-8 nanoparticles demonstrate good thermal stability and water stability, and improved porosity compared to pristine ZIF-8. The

partial replacement of Zn $^{2+}$  with Ni $^{2+}$  introduces valuable properties, creating a robust and adaptable platform for efficient xenon entrapment and significant enhancement of the  $^{129}\text{Xe}$  NMR signal.

### Investigation of the xenon entrapment capability of MOF

When dispersed in water, solvent-free NiZn-ZIF-8 nanoparticles formed a uniform and stable colloidal solution (Supplementary Fig. 62). Hyperpolarized  $^{129}\text{Xe}$  NMR spectra of this dispersion (5 mg mL $^{-1}$ ) revealed two distinct peaks: one at 193.4 ppm, corresponding to dissolved  $^{129}\text{Xe}$  in the aqueous phase, and another at 82.2 ppm, representing  $^{129}\text{Xe}$  trapped within the pores of NiZn-ZIF-8 (Supplementary Fig. 63). Additionally, a third peak at 84.1 ppm, observed in the solid state, indicates that NiZn-ZIF-8 retains its dry micropores even when dispersed in a liquid colloidal environment.

Incorporating nickel into the ZIF-8 framework had minimal impact on the chemical shift of entrapped  $^{129}\text{Xe}$ , but it significantly affected signal intensity (integrated peak area) (Supplementary Fig. 64). The signal intensity increased with rising nickel content but decreased beyond a critical threshold (Fig. 2e). This may be due to two

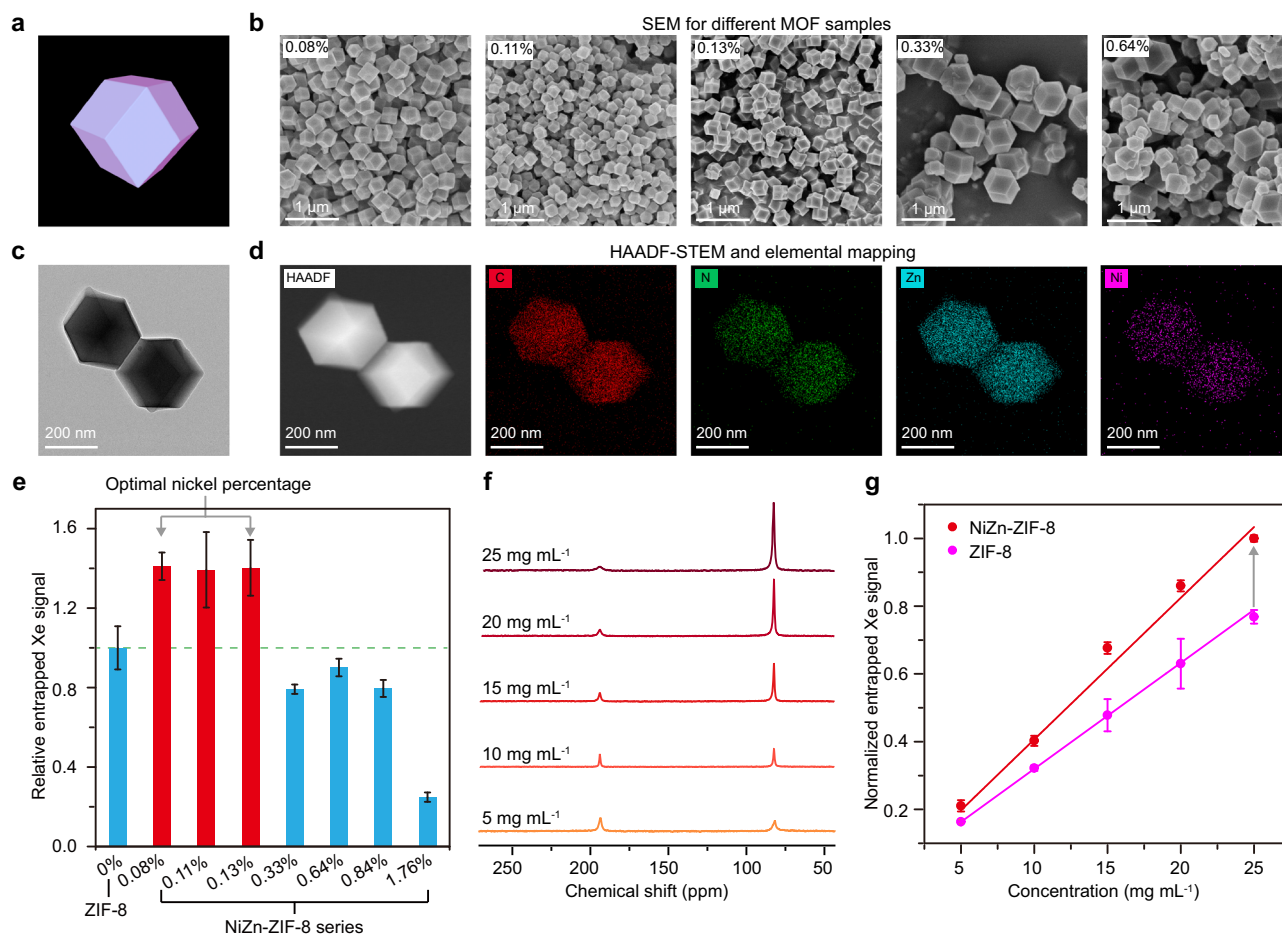


**Fig. 2 | Morphology and hyperpolarized  $^{129}\text{Xe}$  NMR performance of NiZn-ZIF-8.**

**a** Schematic representation of the NiZn-ZIF-8 crystal structure. **b** SEM images of NiZn-ZIF-8 nanoparticles showing consistent dodecahedral morphology across samples (scale bars: 1  $\mu\text{m}$ ). **c** TEM images of NiZn-ZIF-8 (0.08% nickel), illustrating uniform particle size and structure (scale bar: 200 nm). **d** High-angle annular dark-field scanning transmission electron microscopy (HAADF-STEM) and elemental mapping of Ni and Zn within the nanoparticles (scale bars: 200 nm). **e** Relative  $^{129}\text{Xe}$  NMR signal intensities for NiZn-ZIF-8, pristine ZIF-8, and other MOF samples, demonstrating the superior signal enhancement achieved by NiZn-ZIF-8 ( $n = 3$  independent

experimental replicates). **f** Hyperpolarized  $^{129}\text{Xe}$  NMR spectra of NiZn-ZIF-8 nanoparticles (0.08% nickel) at various concentrations (5.0, 10, 15, 20, and 25  $\text{mg mL}^{-1}$ ) in aqueous solutions, showing a concentration-dependent increase in signal intensity. **g** Normalized  $^{129}\text{Xe}$  NMR signal intensities for NiZn-ZIF-8 (red) and pristine ZIF-8 (purple) as a function of MOF concentration, indicating that NiZn-ZIF-8 exhibits a  $\approx 33\%$  greater xenon entrapment capacity compared to pristine ZIF-8 ( $n = 3$  independent experimental replicates). All NMR spectra were acquired using a zg pulse sequence (rectangular pulse,  $p_1 = 31.8 \mu\text{s}$ ), with a single scan (NS = 1) and line broadening (LB = 10 Hz). Data in (e, g) were presented as mean values  $\pm$  SD. Source data are provided as a Source Data file.

key factors: 1) Paramagnetic effects of nickel, which shorten  $^{129}\text{Xe}$   $T_1$  relaxation times (Supplementary Fig. 65, Supplementary Table 6). 2) Reduced dispersity and non-uniform particle morphology at higher nickel concentrations (Fig. 2b, Supplementary Figs. 2-8).

Through optimization, the ideal range for nickel substitution was identified as 0.08%–0.13%. At an optimal 0.08% nickel content, NiZn-ZIF-8 achieved a  $^{129}\text{Xe}$  NMR signal intensity that was 212-fold higher than dissolved  $^{129}\text{Xe}$  in water (Fig. 1c, e). In biologically relevant culture media containing 10% fetal bovine serum (FBS), the entrapped  $^{129}\text{Xe}$  signal was similarly impressive, showing a 216-fold enhancement compared to dissolved  $^{129}\text{Xe}$  (Fig. 1d, f; for the calculation, see Methods). More importantly, although NiZn-ZIF-8 is in blood plasma solutions, the entrapped  $^{129}\text{Xe}$  NMR signal remains strong (Supplementary Fig. 66), making it promising for potential biological applications.

Further analysis revealed that the  $^{129}\text{Xe}$  NMR signal intensity was directly proportional to the concentration of NiZn-ZIF-8 and pristine ZIF-8 nanoparticles, displaying a clear linear relationship over a concentration range of 1–25  $\text{mg mL}^{-1}$ , without altering the entrapped  $^{129}\text{Xe}$  chemical shift (Fig. 2f, g, Supplementary Fig. 67). Importantly, NiZn-ZIF-8 consistently demonstrated stronger xenon entrapment

compared to pristine ZIF-8, with the slope of the linear fit (0.0418  $\text{mL mg}^{-1}$ ) being  $\approx 33\%$  higher than that of ZIF-8 (0.0313  $\text{mL mg}^{-1}$ ) (Fig. 2g). We calculated that the number of entrapped xenon atoms per nanoparticle is  $3.03 \times 10^7$  for NiZn-ZIF-8 and  $2.29 \times 10^7$  for ZIF-8, respectively. In contrast, ZIF-8 doped with  $\text{Cu}^{2+}$  or  $\text{Co}^{2+}$  did not improve  $^{129}\text{Xe}$  NMR signal intensity (Supplementary Fig. 68).

These findings collectively highlight the superior xenon entrapment capabilities of NiZn-ZIF-8, resulting in a significant boost in  $^{129}\text{Xe}$  NMR signal intensity in solution. The optimized nickel doping enhances xenon concentration properties, positioning NiZn-ZIF-8 as a highly promising and customizable platform for hyperpolarized  $^{129}\text{Xe}$  molecular imaging applications.

#### NiZn-ZIF-8 with good hyperpolarized $^{129}\text{Xe}$ MRI performance

To assess the performance of NiZn-ZIF-8 in hyperpolarized  $^{129}\text{Xe}$  MRI, experiments were carried out using high nanoparticle concentrations in a culture medium. A dual-compartment system was employed, with a 5 mm NMR tube containing a NiZn-ZIF-8 dispersion (40  $\text{mg mL}^{-1}$ ) placed inside a 10 mm NMR tube filled with pure culture medium (Fig. 3a). Proton MRI showed strong signal intensity in the 5 mm tube,

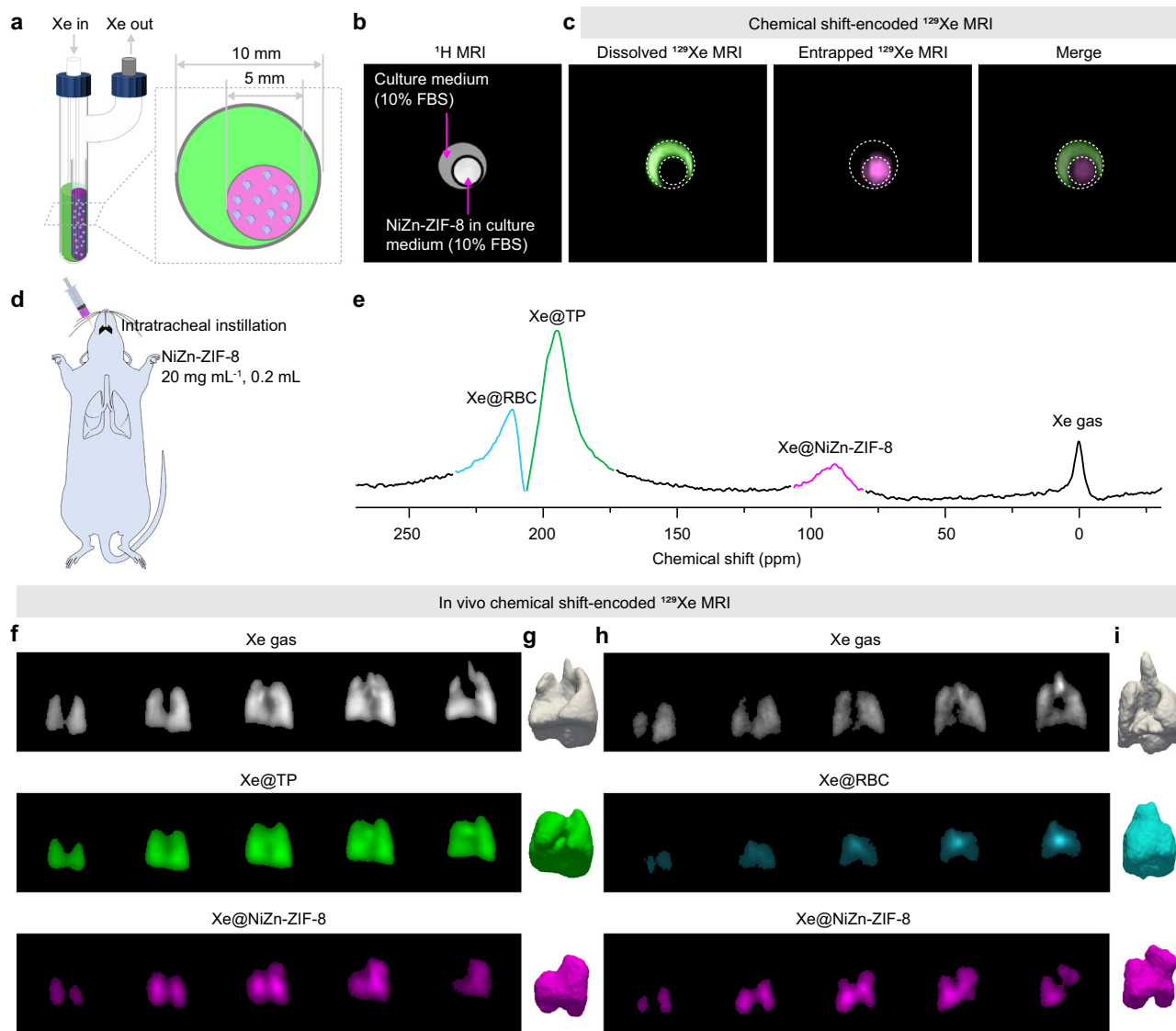


**Fig. 3 | Hyperpolarized  $^{129}\text{Xe}$  MRI performance of NiZn-ZIF-8 (nickel percentage 0.08%) at high concentrations.** **a** Schematic illustration of the NMR tube setup used in the experiment, consisting of a 5 mm inner tube containing NiZn-ZIF-8 dispersion ( $40\text{ mg mL}^{-1}$ ) and a 10 mm outer tube containing pure culture medium. **b** Proton MRI images showing weak signal intensity in the 10 mm tube (culture medium) and strong signal intensity in the 5 mm tube, attributed to proton relaxation enhancement by NiZn-ZIF-8. **c** Chemical shift-encoded hyperpolarized  $^{129}\text{Xe}$  MRI results for NiZn-ZIF-8, demonstrating the separation of dissolved  $^{129}\text{Xe}$  (193.4 ppm) and entrapped  $^{129}\text{Xe}$  (82.2 ppm) signals into distinct colors without interference. **d** Schematic illustration of the intratracheal instillation of NiZn-ZIF-8 solution in rats ( $20\text{ mg mL}^{-1}$ , 0.2 mL). **e** In vivo hyperpolarized  $^{129}\text{Xe}$  NMR spectrum

exhibits a strong  $^{129}\text{Xe}$  NMR signal entrapped by NiZn-ZIF-8, demonstrating its xenon entrapment capability in biological systems. **f** Hyperpolarized  $^{129}\text{Xe}$  images of a rat after NiZn-ZIF-8 instillation clearly show the signal of xenon entrapped by NiZn-ZIF-8 (purple), xenon dissolved in TP (green), and xenon gas (gray). **g** 3D images reconstructed from the simultaneous imaging of xenon gas (gray), xenon entrapped within NiZn-ZIF-8 (purple), and xenon dissolved in TP (green). **h** Hyperpolarized  $^{129}\text{Xe}$  images of a rat after NiZn-ZIF-8 instillation clearly show the signal of xenon entrapped by NiZn-ZIF-8 (purple), xenon dissolved in RBC (cyan), and xenon gas (gray). **i** 3D images reconstructed from the simultaneous imaging of xenon gas, xenon entrapped within NiZn-ZIF-8, and xenon dissolved in RBC.

attributed to proton relaxation enhancement caused by NiZn-ZIF-8, while the outer tube displayed much weaker signal intensity (Fig. 3b). In hyperpolarized  $^{129}\text{Xe}$  MRI, the culture medium alone produced a signal corresponding to dissolved  $^{129}\text{Xe}$ . In contrast, the NiZn-ZIF-8 dispersion showed no detectable signal for dissolved  $^{129}\text{Xe}$ , indicating strong xenon entrapment and relaxation effects. Instead, a distinct and intense signal was observed for entrapped  $^{129}\text{Xe}$  (Fig. 3c). Notably, the signals for dissolved and entrapped xenon were clearly separated, eliminating any signal interference.

To investigate the imaging performance of NiZn-ZIF-8 in vivo, hyperpolarized  $^{129}\text{Xe}$  NMR and MRI were conducted following the intratracheal instillation of NiZn-ZIF-8 solution ( $20\text{ mg mL}^{-1}$ , 0.2 mL) in rats (Fig. 3d-g). Hyperpolarized  $^{129}\text{Xe}$  NMR spectra revealed four

characteristic signal peaks: the peak at 0 ppm corresponded to xenon gas, the peak at 90 ppm to the entrapped  $^{129}\text{Xe}$  within NiZn-ZIF-8, and the peaks at 195 and 212 ppm to the dissolved  $^{129}\text{Xe}$  in tissue and plasma (TP), and red blood cells (RBC), respectively (Fig. 3e). Because of the strong entrapped xenon signal and its chemical shift being far from that of xenon gas and dissolved xenon, simultaneous imaging of xenon gas, dissolved xenon, and entrapped xenon in the lungs was achieved. The signals were clearly observed and distinguished (Fig. 3f-i). Notably, even with just 4 mg of NiZn-ZIF-8 nanoparticles, the entrapped xenon signal was sufficiently strong for analysis, demonstrating the good chemical shift-encoded  $^{129}\text{Xe}$  MRI performance of NiZn-ZIF-8 in vivo. This highlights the great potential of NiZn-ZIF-8 for future biological applications.

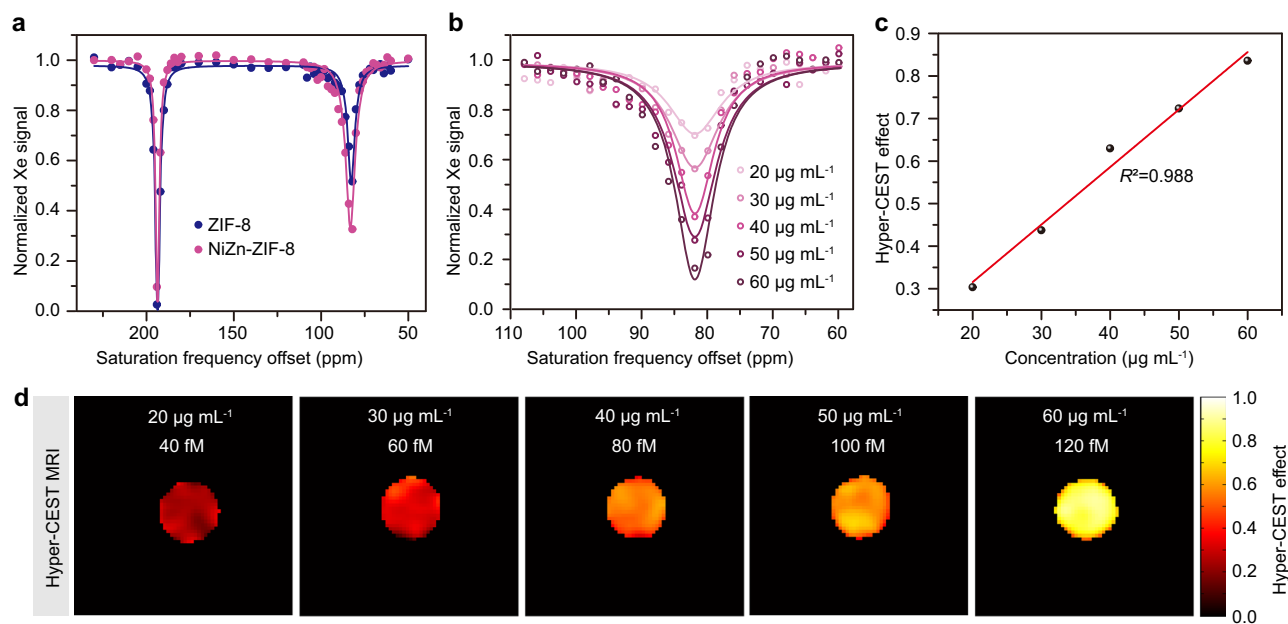


**Fig. 4 | Hyperpolarized  $^{129}\text{Xe}$  NMR and MRI performance of NiZn-ZIF-8 (nickel percentage 0.08%) at low concentrations. a** Hyper-CEST spectra comparing NiZn-ZIF-8 (purple circle) and pristine ZIF-8 (blue circle) at the same concentration ( $40\ \mu\text{g mL}^{-1}$ ), showing a stronger Hyper-CEST effect for NiZn-ZIF-8. **b** Hyper-CEST spectra of NiZn-ZIF-8 at varying concentrations ( $20, 30, 40, 50,$  and  $60\ \mu\text{g mL}^{-1}$ ) in aqueous solutions, highlighting the concentration-dependent increase in signal

intensity. **c** Plot of the Hyper-CEST effect at  $82\ \text{ppm}$  as a function of NiZn-ZIF-8 concentration, demonstrating a linear relationship over the range of  $20\text{--}60\ \mu\text{g mL}^{-1}$ . **d** Hyper-CEST MRI phantom images of NiZn-ZIF-8 at different concentrations, illustrating the dose-dependent enhancement in MRI signal intensity. Source data are provided as a Source Data file.

The xenon entrapment ability of NiZn-ZIF-8 and ZIF-8 was further analyzed using the hyperpolarized xenon chemical exchange saturation transfer (Hyper-CEST) method<sup>16</sup>. Both NiZn-ZIF-8 and pristine ZIF-8 exhibited a saturation response centered around  $82\ \text{ppm}$ . However, at an equivalent concentration of  $40\ \mu\text{g mL}^{-1}$ , NiZn-ZIF-8 demonstrated a significantly stronger Hyper-CEST effect compared to pristine ZIF-8, aligning with the results observed in direct  $^{129}\text{Xe}$  NMR measurements (Fig. 4a).

Further Hyper-CEST experiments conducted across a range of NiZn-ZIF-8 concentrations ( $20\text{--}60\ \mu\text{g mL}^{-1}$ ) revealed a clear linear relationship between the Hyper-CEST effect and nanoparticle concentration (Fig. 4b, c). Remarkably, even at a low concentration of  $20\ \mu\text{g mL}^{-1}$ , NiZn-ZIF-8 achieved a Hyper-CEST effect of  $\approx 30\%$ , highlighting its capability to trap xenon. Corresponding Hyper-CEST MRI also demonstrated strong signal intensity even at low concentrations of NiZn-ZIF-8 nanoparticles, with intensity measurements showed a strong linear relationship with NiZn-ZIF-8 concentration (Fig. 4d, Supplementary Figs. 69, 70).

To determine the detection threshold, time-dependent saturation transfer spectra were collected for serial dilutions of NiZn-ZIF-8 at  $100, 10, 2,$  and  $1\ \mu\text{g mL}^{-1}$  (Supplementary Fig. 71). The detection threshold was identified as  $2\ \mu\text{g mL}^{-1}$ , which corresponds to a low concentration of  $\approx 4\ \text{fM}$ , calculated using nanoparticle tracking analysis. The detection threshold of pristine ZIF-8 was identified as  $3\ \mu\text{g mL}^{-1}$  by the same method (Supplementary Fig. 72). The detection threshold of NiZn-ZIF-8 is about 25 times lower than that of nanoemulsion droplets ( $100\ \text{fM}$ )<sup>42</sup>, and about 6250 times lower than that of the gas vesicles ( $25\ \text{pM}$ )<sup>43</sup>. This represents the lowest concentration of detected xenon hosts of nanomaterials to date, marking a significant advancement in hyperpolarized  $^{129}\text{Xe}$  NMR field (Supplementary Table 7)<sup>42–46</sup>.

NiZn-ZIF-8 proves to be an effective xenon host, capable of concentrating xenon atoms with unmatched sensitivity and significantly boosting  $^{129}\text{Xe}$  NMR signals in aqueous solutions. These results underscore its potential for hyperpolarized  $^{129}\text{Xe}$  MRI at low

concentrations, positioning it as a powerful tool for advanced molecular imaging and diagnostic applications.

### Investigation of xenon interactions within the MOF pores

The role of nickel ions in influencing xenon interactions within the NiZn-ZIF-8 pores was studied using variable-temperature hyperpolarized  $^{129}\text{Xe}$  NMR and two-dimensional  $^{129}\text{Xe}$  exchange spectroscopy (2D EXSY). In aqueous solutions containing NiZn-ZIF-8, the chemical shift of dissolved  $^{129}\text{Xe}$  showed a nonlinear temperature dependence: it increased with temperature up to  $300\ \text{K}$  and then decreased at higher temperatures (Fig. 5a, Supplementary Fig. 73). A similar trend was observed for pure water and pristine ZIF-8 (Fig. 5a). In contrast, the chemical shift of entrapped  $^{129}\text{Xe}$  within NiZn-ZIF-8 exhibited a linear relationship with temperature over the range of  $278\text{--}320\ \text{K}$ . The slope and intercept for NiZn-ZIF-8 were  $-0.0731 \pm 0.0004\ \text{ppm K}^{-1}$  and  $103.98 \pm 0.12\ \text{ppm}$ , respectively, compared to  $-0.0759 \pm 0.0012\ \text{ppm K}^{-1}$  and  $104.51 \pm 0.36\ \text{ppm}$  for pristine ZIF-8. These slight differences suggest that the incorporation of nickel into the framework alters the interactions between xenon and the MOF pore environment, fine-tuning its properties. Interestingly, the temperature-dependent behavior of entrapped  $^{129}\text{Xe}$  in NiZn-ZIF-8 differs from molecular cages like cryptophane and metal-organic capsules<sup>47–51</sup>, which typically trap only a single xenon atom per cavity. In contrast, MOFs can hold multiple xenon atoms within each pore, allowing xenon-xenon interactions to influence the NMR signal. At higher temperatures, the increased thermal motion of xenon atoms reduces their residence time within the pores and weakens xenon-xenon interactions, leading to upfield shifts in the  $^{129}\text{Xe}$  NMR signal.

The dynamics of xenon exchange between the entrapped and dissolved states were examined using 2D EXSY (Supplementary Figs. 74–81). For the NiZn-ZIF-8, at a  $0\ \text{ms}$  mixing time, no cross peaks were observed, indicating that no exchange occurred between the two states (Supplementary Fig. 76a). However, at a  $1.5\ \text{ms}$  mixing time, cross peaks appeared, confirming chemical exchange between the entrapped and dissolved xenon (Fig. 5c). By fitting the peak intensities

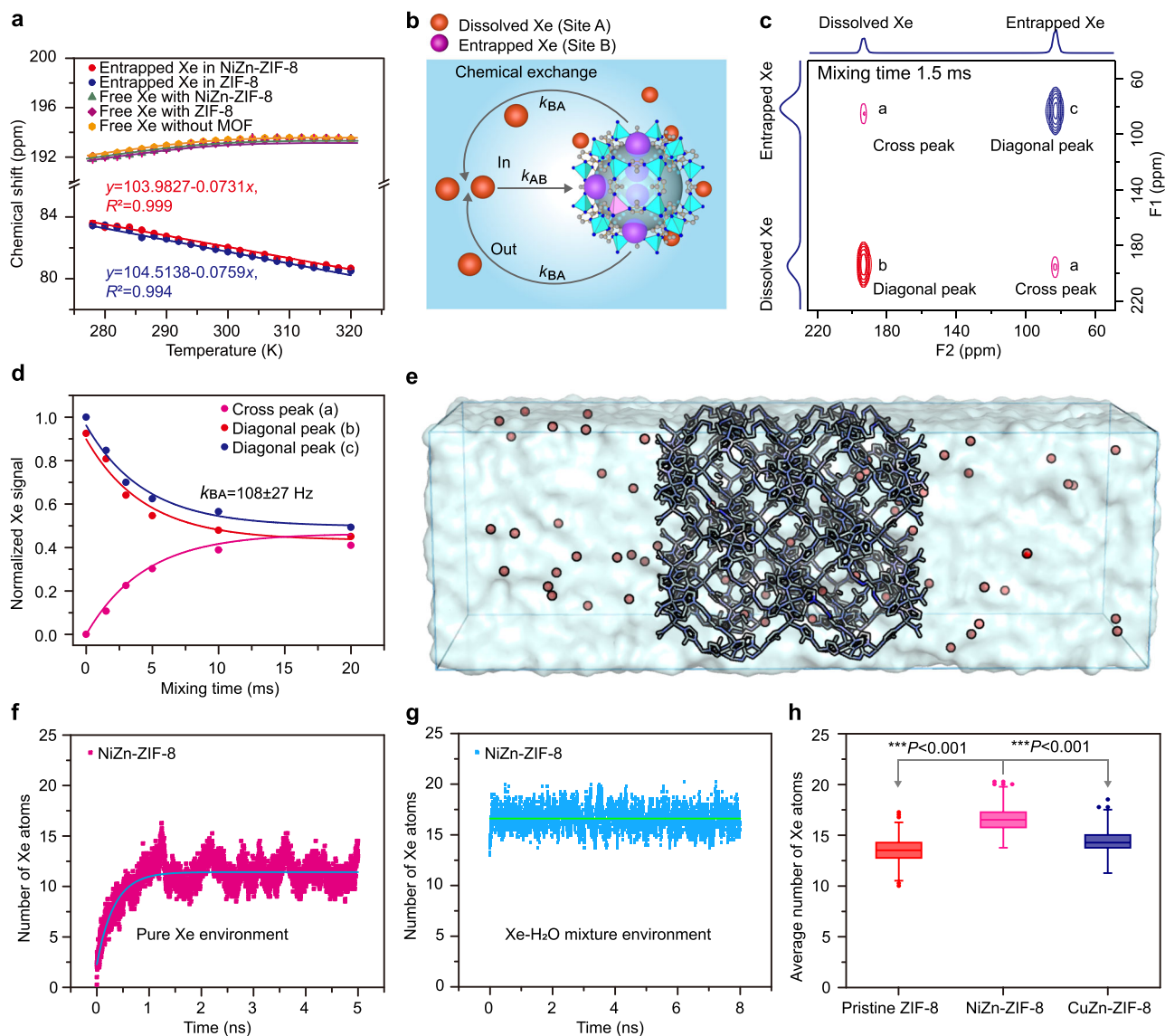


**Fig. 5 | Temperature-dependent hyperpolarized  $^{129}\text{Xe}$  NMR, 2D  $^{129}\text{Xe}$  EXSY spectra, and MD simulations.** **a** Temperature dependence of hyperpolarized  $^{129}\text{Xe}$  chemical shift for dissolved  $^{129}\text{Xe}$  in water, pristine ZIF-8, and NiZn-ZIF-8. Dissolved  $^{129}\text{Xe}$  exhibits nonlinear behavior, while entrapped  $^{129}\text{Xe}$  in NiZn-ZIF-8 shows a linear trend ( $n = 3$  independent experimental replicates). **b** Schematic illustration of the chemical exchange process between dissolved  $^{129}\text{Xe}$  and entrapped  $^{129}\text{Xe}$  within NiZn-ZIF-8 pores. **c** 2D  $^{129}\text{Xe}$  EXSY spectrum of NiZn-ZIF-8 at a mixing time of 1.5 ms, showing cross peaks indicative of xenon exchange between dissolved and entrapped states. **d** Exchange rate determination: Cross peak (purple circle), diagonal peak of dissolved  $^{129}\text{Xe}$  (red circle), and diagonal peak of entrapped  $^{129}\text{Xe}$  (blue circle) intensities from 2D  $^{129}\text{Xe}$  EXSY as a function of mixing time, fitted to a two-site exchange model, yielding a chemical exchange rate of  $108 \pm 27$  Hz for NiZn-ZIF-8. **e** MD simulation setup: Snapshot of the simulation box ( $34 \times 34 \times 102 \text{ \AA}^3$ ) after equilibration, containing NiZn-ZIF-8 surrounded by 600  $\text{H}_2\text{O}$  molecules and 60 xenon atoms. Xenon atoms are shown in

red; carbon, light gray; hydrogen, white; nitrogen, blue; and metal, light blue.  $\text{H}_2\text{O}$  molecules are represented as a semi-transparent gray volume. **f, g** Xenon entrapment dynamics: Change in the number of xenon atoms entrapped by NiZn-ZIF-8 in **(f)** pure xenon and **(g)** xenon-water environments over the simulation timescale, demonstrating higher xenon entrapment in the xenon-water mixture. **h** Average xenon entrapment: MD simulation results showing the mean number of xenon atoms entrapped in pristine ZIF-8 (red box), NiZn-ZIF-8 (purple box), and CuZn-ZIF-8 (blue box) during the final 5 ns of the simulation in the xenon-water environment. NiZn-ZIF-8 exhibits significantly higher xenon entrapment.  $n = 5001$  independent data points. The box plots show the interquartile range, with the centre lines indicating the medians and the whiskers the minimum and maximum values. Data in **(a)** were presented as mean values  $\pm$  SD. Statistical significance was calculated using unpaired two-tailed Student's *t*-test. Source data are provided as a Source Data file.

over time to a two-site exchange model<sup>52</sup>, the exchange rate for NiZn-ZIF-8 was determined to be  $108 \pm 27$  Hz (Fig. 5d). In comparison, pristine ZIF-8 and CuZn-ZIF-8 showed faster exchange rates of  $124 \pm 27$  Hz and  $214 \pm 48$  Hz, respectively (Supplementary Figs. 77–81). The slower exchange rate in NiZn-ZIF-8 indicates that nickel incorporation enhances the MOF's affinity for xenon, reducing the rate of exchange between the entrapped and dissolved states. This increased affinity

aligns with the observed improvements in xenon entrapment and the enhanced  $^{129}\text{Xe}$  NMR signal intensity.

### Xenon adsorption isotherms

Xenon adsorption isotherms were performed at 298 and 273 K to investigate the interaction strength between the xenon and the framework (Supplementary Fig. 82). We found that the xenon uptake

amounts of NiZn-ZIF-8 is consistent with the pristine ZIF-8, but the isosteric heats of adsorption ( $Q_{st}$ ) of xenon in the framework is different. The  $Q_{st}$  of xenon at nearly zero loadings for NiZn-ZIF-8 and ZIF-8 are estimated to be 16.93 and 16.83 kJ mol<sup>-1</sup>, respectively (Supplementary Figs. 83, 84). The  $Q_{st}$  of xenon in the NiZn-ZIF-8 is slightly higher than that of pristine ZIF-8, demonstrating that the xenon atoms have a higher affinity with the NiZn-ZIF-8. Therefore, the nickel in the framework may play a key role in enhancing the affinity between the xenon and the framework.

### Molecular dynamics simulations

To gain deeper insight into xenon entrapment, molecular dynamics (MD) simulations were conducted for NiZn-ZIF-8, CuZn-ZIF-8, and pristine ZIF-8 (Fig. 5e–h, Supplementary Movie 1, and Supplementary Figs. 85–90). Snapshots taken every 1.0 ps along the simulation trajectory quantified the number of xenon atoms trapped within the MOF pores. The simulations revealed that xenon was rapidly entrapped in both pure xenon and xenon-water environments (Fig. 5f, g). In the pure xenon environment, the average number of xenon atoms trapped by NiZn-ZIF-8 has no significant difference compared with pristine ZIF-8 and CuZn-ZIF-8 (Fig. 5f, Supplementary Figs. 87, 88). This is consistent with the xenon adsorption isotherms (Supplementary Fig. 82). While in the xenon-water mixture (Fig. 5g, Supplementary Fig. 89), NiZn-ZIF-8 showed a significantly higher average number of trapped xenon atoms (16.6) compared to pristine ZIF-8 (13.4) and CuZn-ZIF-8 (14.4) (Fig. 5h). Notably, the number of xenon atoms trapped in the xenon-water mixture was significantly higher than in the pure xenon environment. This result indicates that the MOF pores remain hydrophobic even when dispersed in water, allowing xenon atoms to preferentially occupy the pore interiors rather than dissolving into the surrounding water.

From MD simulations, we calculated the distances between xenon and metal atoms for each snapshot. The free-energy profiles were determined by analyzing the probability distributions of these distances (Supplementary Fig. 90). The results indicate that the free-energy minima for pristine ZIF-8, CuZn-ZIF-8, and NiZn-ZIF-8 occur at a distance of 5.8 Å. However, the depth of the free-energy profiles varies: -24.78 kJ mol<sup>-1</sup> for pristine ZIF-8, -24.87 kJ mol<sup>-1</sup> for CuZn-ZIF-8, and -25.16 kJ mol<sup>-1</sup> for NiZn-ZIF-8. These findings suggest that NiZn-ZIF-8 exhibits a stronger ability to trap the xenon atoms compared to both pristine ZIF-8 and CuZn-ZIF-8, as indicated by the deeper free-energy minimum.

These results confirm that incorporating nickel into the framework enhances the material's affinity for xenon, resulting in increased xenon entrapment. This improved trapping capability directly explains the enhanced <sup>129</sup>Xe NMR signal intensity observed for NiZn-ZIF-8. In summary, incorporating nickel into the ZIF-8 framework significantly improves its affinity for xenon and increases the number of trapped xenon atoms, providing a dual advantage for molecular imaging. The enhanced BET surface area and superior xenon retention make NiZn-ZIF-8 a suitable material for concentrating xenon and amplifying NMR signals in aqueous solutions.

### Discussion

This study demonstrates that NiZn-ZIF-8, developed through a MTV-MOF strategy, serves as an effective platform for enhancing hyperpolarized <sup>129</sup>Xe NMR signal intensity in aqueous environments. By incorporating nickel into the ZIF-8 framework, we created a material with greater xenon affinity, improved xenon trapping capacity, and extended xenon residence time within its pores. These advancements led to a ~33% increase in <sup>129</sup>Xe NMR signal intensity compared to pristine ZIF-8 and a 210-fold enhancement relative to dissolved xenon in water and biological media. NiZn-ZIF-8 also excels as a chemical shift-encoded MRI reporter, precisely distinguishing between dissolved and entrapped xenon signals, and demonstrates good chemical

shift-encoded MRI performance in rat lungs. With a detection threshold of ~4 fM, enabling the detection of trace molecules using HyperCEST MRI. These findings highlight NiZn-ZIF-8's immense potential for advanced molecular imaging in complex biological systems, addressing critical challenges in signal intensity and sensitivity faced by existing probes.

This MTV strategy opens up broader opportunities to design next-generation MOFs with customizable properties. This expands their potential applications beyond <sup>129</sup>Xe MRI into fields such as biomedical imaging, optics, and electronics. By showcasing how strategic compositional tuning can unlock new functionalities, this work marks a significant advancement in the development of functional MOFs for transformative applications in molecular imaging and diagnostics. In the future, the chemical shift-encoded reporter, NiZn-ZIF-8, will be functionalized with targeting moieties such as hyaluronic acid, RGD, or other relevant targeting moieties. When targeting-functionalized NiZn-ZIF-8 is combined with hyperpolarized <sup>129</sup>Xe, it could enable targeted molecular imaging *in vivo*, particularly for the detection of diseases. For example, in the context of pulmonary diseases like lung cancer, hyperpolarized <sup>129</sup>Xe combined with NiZn-ZIF-8 could provide imaging of the lungs, overcoming the low sensitivity challenges typically associated with conventional imaging agents.

## Methods

### Materials

Zinc acetate dehydrate (Analytical reagent, 99.7%), nickel acetate tetrahydrate, zinc nitrate hexahydrate (Analytical reagent, 99.7%), nickel nitrate hexahydrate (Analytical reagent, 99.7%), copper acetylacetonate (Analytical reagent, 99.7%), cobalt acetylacetonate (Analytical reagent, 99.7%), anhydrous methanol (Analytical reagent, 99.7%) were purchased from Sinopharm Chemical Reagent Co., Ltd. (Shanghai, China). 2-methyl-imidazole (mIM, 98%) was purchased from Aladdin. All chemicals were used as received without further purification unless otherwise stated.

### Characterization

Characterization of the synthesized materials was conducted using a variety of techniques to assess their structural and thermal properties, as well as their morphology and elemental composition. Brunauer–Emmett–Teller (BET) surface area and pore size measurements were carried out through nitrogen adsorption and desorption isotherms at 77 K using a Micromeritics 3Flex 5.0 instrument. Powder X-ray diffraction (PXRD) patterns were recorded on a Bruker D8 (3 kW) diffractometer to confirm the crystallinity and phase purity of the samples. Thermal stability was evaluated using thermogravimetric analysis and differential scanning calorimetry (TGA-DSC) on a Mettler TG-DSC 3+ instrument in an air atmosphere over a temperature range of 30–800 °C, with a controlled air flow rate of 60 mL min<sup>-1</sup>.

The size and morphology of the MOF nanoparticles were examined using high-resolution SEM equipped with energy-dispersive X-ray spectroscopy (EDX) and TEM performed on an FEI Titan transmission electron microscope operating at 200 kV. Elemental mapping was conducted using scanning transmission electron microscopy (STEM) with a high-angle annular dark-field (HAADF) detector to confirm the homogeneous distribution of elements within the MOF frameworks. Additionally, elemental analysis was performed using inductively coupled plasma optical emission spectroscopy (ICP-OES) with an ICPOES760 instrument (Agilent) to quantify the elemental composition of the samples.

### Synthesis of pristine ZIF-8

To synthesize pristine ZIF-8, zinc acetate dihydrate (Zn(OAc)<sub>2</sub> · 2H<sub>2</sub>O, 542.2 mg, 2.47 mmol) and mIM (810.6 mg, 9.87 mmol) were each dissolved in 50 mL of MeOH in separate 250 mL conical flasks. The dissolution was aided by ultrasound to ensure complete solubilization of

the reagents. The mM solution was then poured into the zinc acetate solution under vigorous stirring, and mixing was continued until the solutions were fully combined. Stirring was stopped, and the resulting mixture was allowed to stand undisturbed for 24 h. A white precipitate formed during this time was recovered by centrifugation. The collected product was washed three times with MeOH to remove any unreacted metal salts or ligands, yielding the final ZIF-8 material.

### Synthesis of NiZn-ZIF-8

To synthesize NiZn-ZIF-8, nickel acetate tetrahydrate ( $\text{Ni}(\text{OAc})_2 \cdot 4\text{H}_2\text{O}$ , 49.7 mg, 0.2 mmol) and zinc acetate dihydrate ( $\text{Zn}(\text{OAc})_2 \cdot 2\text{H}_2\text{O}$ , 175.6 mg, 0.8 mmol) were dissolved separately in 50 mL of MeOH with the help of ultrasound in a 250 mL conical flask. Simultaneously, mM (656 mg, 8 mmol) was dissolved in 50 mL of MeOH in a separate 250 mL conical flask using ultrasound. The mM solution was then added to the metal acetate solution under vigorous stirring. Stirring was continued for 3 h, after which the mixture was allowed to stand undisturbed for 24 h. The precipitate formed was collected by centrifugation and washed three times with MeOH to remove any unreacted metal salts or ligands. Samples of NiZn-ZIF-8 with varying nickel percentages were synthesized using the same procedure by altering the molar ratio of  $n(\text{Ni}(\text{OAc})_2 \cdot 4\text{H}_2\text{O})/n(\text{Zn}(\text{OAc})_2 \cdot 2\text{H}_2\text{O})$ , while maintaining the total moles of the two metal salts at 1 mmol. The resulting nickel percentages in the MOF samples were as follows: for  $n(\text{Ni}(\text{OAc})_2 \cdot 4\text{H}_2\text{O})/n(\text{Zn}(\text{OAc})_2 \cdot 2\text{H}_2\text{O}) = 1/3 \cong 0.11\%$  nickel;  $1/2 \cong 0.13\%$  nickel;  $1/1 \cong 0.33\%$  nickel;  $2/1 \cong 0.64\%$  nickel;  $3/1 \cong 0.84\%$  nickel; and  $4/1 \cong 1.76\%$  nickel.

### Synthesis of CuZn-ZIF-8

Copper-substituted ZIF-8 (CuZn-ZIF-8) was synthesized using a procedure similar to that for NiZn-ZIF-8. Copper acetylacetonate ( $\text{Cu}(\text{AcAc})_2$ ) (52.4 mg, 0.2 mmol) and zinc acetate dihydrate ( $\text{Zn}(\text{OAc})_2 \cdot 2\text{H}_2\text{O}$ ) (175.6 mg, 0.8 mmol) were dissolved in 50 mL of MeOH using ultrasound. Separately, mM (656 mg, 8 mmol) was dissolved in 50 mL of MeOH with ultrasound. The mM solution was then poured into the copper and zinc solution under vigorous stirring, which was continued for 3 h. The mixture was left to stand undisturbed for 24 h, and the precipitate was collected by centrifugation. The product was washed three times with MeOH to remove unreacted salts and ligands. ICP-OES analysis indicated that the copper content in the CuZn-ZIF-8 sample was 0.06%.

### Synthesis of CoZn-ZIF-8

Cobalt-substituted ZIF-8 (CoZn-ZIF-8) was synthesized by dissolving cobalt acetylacetonate ( $\text{Co}(\text{AcAc})_2$ ) (4.97 mg, 0.02 mmol) and zinc acetate dihydrate ( $\text{Zn}(\text{OAc})_2 \cdot 2\text{H}_2\text{O}$ , 215.1 mg, 0.98 mmol) in 50 mL of MeOH using ultrasound in a 250 mL conical flask. Separately, mM (656 mg, 8 mmol) was dissolved in 50 mL of MeOH in another 250 mL conical flask with the aid of ultrasound. The mM solution was then poured into the cobalt-zinc solution under vigorous stirring, which was continued for 3 h. The mixture was allowed to stand undisturbed for 24 h, and the resulting precipitate was recovered by centrifugation. The product was washed three times with MeOH to remove any unreacted metal salts and ligands. ICP-OES analysis indicated that the cobalt percentage in the CoZn-ZIF-8 sample was 0.33%.

### Sample activation procedures for NiZn-ZIF-8

The as-synthesized NiZn-ZIF-8 samples were activated to remove residual solvents. The samples were first centrifuged and washed three times with anhydrous MeOH to exchange the pore solvent. The MeOH-exchanged samples were transferred as a suspension to a quartz cell, and the solvent was decanted. The remaining MeOH within the pores was removed by evacuating the samples under vacuum ( $10^{-2}$  Torr) at room temperature for 12 h. This was followed by heating the samples

to 120 °C at a controlled rate of 1 °C min<sup>-1</sup> for 12 h. The same controlled rate was applied during the subsequent cooling process.

### ICP-OES analysis

The elemental content of zinc, nickel, copper, and cobalt in the MOF samples was quantified using ICP-OES. For a typical analysis, 5 mg of the MOF sample was added to 10 mL of a 4% nitric acid ( $\text{HNO}_3$ ) aqueous solution. The mixture was sonicated for 10 min and then heated to 100 °C for 2 h to ensure complete digestion. After cooling to room temperature, the resulting solution was diluted to a total volume of 10 mL and filtered using a 0.22 μm filter to remove particulates. Standard solutions containing 1, 5, 10, 20, 50, 100, and 200 ppm of nickel, copper, cobalt, or zinc in 3% nitric acid were prepared. A calibration curve was generated by plotting chromatographic peak intensities against the known concentrations of the standards, enabling precise quantification of the metal content in the MOF samples.

### Thermal gravimetric analysis

TGA measurements were performed using a TGA analyzer, with samples placed in aluminum oxide pans under a continuous airflow atmosphere. The balance gas was nitrogen ( $\text{N}_2$ ) at a flow rate of 40.0 mL min<sup>-1</sup>, and the sample gas was air at a flow rate of 60.0 mL min<sup>-1</sup>. Samples were heated at a constant rate of 10 °C min<sup>-1</sup> during all TGA experiments.

### N<sub>2</sub> adsorption analysis

All N<sub>2</sub> adsorption experiments were carried out on a Micromeritics 3 Flex automatic volumetric instrument. Measurements were performed at 77 K using a liquid nitrogen bath. Ultra-high purity N<sub>2</sub> was used as the adsorbate. Prior to isotherm measurements, ZIF-8 and the series of NiZn-ZIF-8 samples were degassed on the 3 Flex instrument for 10 h at 120 °C. Pore size distributions for the MOFs were analyzed using quenched NLDFT with a carbon slit-pore model.

### PXRD crystallography

PXRD data for MOF samples were collected using a Bruker D8 3 kW diffractometer with  $\text{Cu-K}\alpha$  X-ray radiation ( $\lambda = 1.5406 \text{ \AA}$ ) in transmission geometry.

### MOF nanoparticle concentration analysis

NiZn-ZIF-8 nanoparticles (2 mg) were dispersed in 40 mL of pure water and sonicated for 5 min. A 1 mL aliquot of this stock solution was then diluted to 3 mL with pure water and sonicated for an additional 5 min. The nanoparticle concentration in the diluted solution was analyzed using a nanoparticle tracking analysis (NTA) system (ZetaView PMX 110). The measurements were performed at a controlled temperature of 23 to 30 °C. The particle concentration was converted to molar concentration using the formula (molar concentration = particle concentration/ $N_A$ ,  $N_A$  is Avogadro's constant).

### Animal preparation

All procedures were approved by the Review Board of the Innovation Academy for Precision Measurement Science and Technology, Chinese Academy of Sciences, and were performed in accordance with the national Regulations for the Administration of Affairs Concerning Experimental Animals. Healthy male and female Sprague–Dawley rats (body mass 240–260 g) were provided by the Hubei Provincial Center for Disease Control and Prevention (Wuhan, Hubei, China). Prior to surgery, the rats were anesthetized with 5% isoflurane (RWD, Shenzhen, Guangdong, China) and maintained under 2% isoflurane anesthesia during the procedure.

## Hyperpolarized $^{129}\text{Xe}$ experiments

Hyperpolarized  $^{129}\text{Xe}$  gas was generated using a commercial  $^{129}\text{Xe}$  hyperpolarizer ( $\approx 40\%$  polarization, verImagin Healthcare, Wuhan, China) in continuous flow mode. All  $^{129}\text{Xe}$  NMR and MRI experiments were performed on a 9.4 T Bruker AV400 wide-bore NMR spectrometer (Bruker Biospin, Ettlingen, Germany) or a 7 T animal MRI scanner (Bruker Biospec 70/20 USR, Billerica, MA, USA) equipped with a home-built dual-tuned birdcage coil.

For hyperpolarized  $^{129}\text{Xe}$  experiments in solution, a gas mixture of 10%  $\text{N}_2$ , 88% He, and 2% Xe (26.4% natural abundance of  $^{129}\text{Xe}$ ) from Spectra Gases was used. The gas mixture was maintained at a pressure of 3.5 bar and flowed at 0.1 SLPM. During experiments, after the gas mixture was polarized, it was bubbled directly into a 10 mm NMR tube containing the MOF sample for 20 or 60 s (single scan). A 3 s delay was allowed to collapse the bubbles before acquiring the spectrum using a zg sequence (rectangular pulse,  $p_1 = 31.8 \mu\text{s}$ ). For variable-temperature experiments, temperatures were varied from 278 to 320 K in 2 K increments. A stabilization time of 10 min was allowed at each temperature before acquiring the  $^{129}\text{Xe}$  NMR spectrum. The sample temperature was controlled using a variable temperature (VT) unit integrated into the NMR spectrometer.  $^{129}\text{Xe}$  NMR chemical shifts were referenced to the signal of gaseous xenon at 0 ppm.

For hyperpolarized  $^{129}\text{Xe}$  MRI experiments in solution, 16 scans were acquired and averaged. Images were collected using a Rapid Acquisition with Relaxation Enhancement (RARE) sequence with the following parameters: slice thickness = 30 mm, matrix size =  $32 \times 32$ , FOV =  $30 \times 30$  mm, in-plane resolution =  $0.9375 \times 0.9375$  mm, bandwidth = 5400 Hz, echo time = 8.5 ms, centric k-space encoding, no partial Fourier transform acceleration, rare factor = 4. For each excitation, the gas mixture was bubbled into the solution for 20 s, followed by a 3 s delay to allow bubble collapse, after which the image was acquired.

For in vivo hyperpolarized  $^{129}\text{Xe}$  experiments, a gas mixture of 10%  $\text{N}_2$ , 88% He, and 2% Xe (86% enriched abundance of  $^{129}\text{Xe}$ ) from Spectra Gases was used. Polarized xenon gas was accumulated and frozen in a magnetic field-protected cold finger using liquid nitrogen, then thawed into a 1.0 L Tedlar bag for delivery to the rats by mechanical ventilation. A 3D Ultra-short Echo Time (UTE) simultaneous imaging sequence was used to obtain images of the dissolved xenon (xenon dissolved in TP or RBC), entrapped xenon, and xenon gas at the same time, with the following parameters: TR = 250 ms, matrix size =  $192 \times 192 \times 192$ , FOV =  $15 \times 15 \times 15$  cm, 1000 projections with Fibonacci trajectory, and the reconstructed spatial resolution =  $0.47 \times 0.47 \times 0.47$  mm. In Hyper-CEST experiments, the hyperpolarized gas mixture was bubbled into a 10 mm NMR tube for 20 s, followed by a 3 s delay for bubble collapse. A continuous wave (cw) pulse ( $6.5 \mu\text{T}$ , 10 s) was applied to saturate xenon within the NiZn-ZIF-8 pores, and the  $^{129}\text{Xe}$  NMR spectrum was subsequently acquired in a single scan. Spectral processing included Lorentzian broadening (LB = 5 Hz).

For detection limit tests, the polarized gas mixture was bubbled into a 10 mm NMR tube for 20 s, followed by a 3 s delay for bubble collapse. A selective saturation pulse was applied, and the spectrum was acquired. The cw-saturation pulses were tuned to either the resonant frequency of xenon within the NiZn-ZIF-8 pores or off-resonance. Saturation times ranged from 0 to 20 s in 1 s increments under a  $13 \mu\text{T}$  field. Spectra were acquired in single scans and processed using Lorentzian broadening (LB = 5 Hz).

For Hyper-CEST MRI experiments, 8 on-resonant and 8 off-resonant scans were acquired and averaged. Images were collected using a RARE sequence with the following parameters: slice thickness = 30 mm, matrix size =  $32 \times 32$ , FOV =  $30 \times 30$  mm, in-plane resolution =  $0.9375 \times 0.9375$  mm, bandwidth = 5400 Hz, echo time = 4.65 ms, centric k-space encoding, no partial Fourier transform acceleration, rare factor = 8. For

each excitation, the gas mixture was bubbled into the solution for 20 s, followed by a 3 s delay to allow bubble collapse. A saturation pulse (6 s,  $13 \mu\text{T}$ ) was applied to saturate xenon within the NiZn-ZIF-8 pores or off-resonance, after which the image was acquired. MR images were processed in MATLAB (R2014a, MathWorks, Natick, MA). The raw  $32 \times 32$  image matrix was interpolated to a  $64 \times 64$  matrix. Hyper-CEST effects for on-resonant saturation were calculated relative to off-resonant saturation using the formula:

$$\text{CEST effect} = \frac{\text{Intensity}_{\text{off}} - \text{Intensity}_{\text{on}}}{\text{Intensity}_{\text{off}}} \quad (1)$$

Point-by-point analysis was performed, and a mask was applied to exclude non-sample areas and regions with normalized signal intensities below 0.2.

## Hyperpolarized $^{129}\text{Xe}$ two-dimensional exchange spectroscopy (2D EXSY)

Hyperpolarized  $^{129}\text{Xe}$  2D EXSY experiments were conducted at 298 K using a  $90^\circ\text{-}t_1\text{-}90^\circ\text{-}t_m\text{-}90^\circ\text{-}t_2$  pulse sequence and the States-TPPI method for phase-sensitive detection in the indirect dimension. The gas mixture was bubbled into the solution for 20 s, followed by a 3 s delay for bubble collapse. The mixing time ( $t_m$ ) was varied from 0 to 20 ms, during which transverse magnetization was eliminated using phase cycling in the pulse sequence. The 2D NMR data were acquired with 32 and 256 points in the  $t_1$  and  $t_2$  dimensions, respectively, with 4 scans per point.

## $T_1$ relaxation measurements for hyperpolarized $^{129}\text{Xe}$

A small flip angle pulse sequence was used to measure the  $T_1$  relaxation time of hyperpolarized  $^{129}\text{Xe}$ . After hyperpolarized gas mixture was bubbled into the solution for 20 s, a 3 s delay was allowed for bubble collapse. A small flip angle non-selective pulse was then applied to the sample, and a free induction decay (FID) was collected immediately after the pulse. The signal was allowed to decay before applying another small flip angle pulse to the remaining magnetization, followed by the collection of another FID. This process was repeated for the desired number of points along the decay curve. The collected signal was fitted to a monoexponential decay model described by the equation:

$$M_t = M_0 \exp\left(-\frac{t}{T_1}\right) \quad (2)$$

where  $M_t$  is the magnetization at time  $t$ ,  $M_0$  is the initial magnetization, and  $T_1$  is the spin-lattice relaxation time.

However, the  $T_1$  measured with this pulse sequence will be shorter than the  $T_1$  measured with a conventional pulse sequence. Every pulse decreases the amount of magnetization, shortening the time needed for the signal to decay to zero. However, the effect of the small flip angle pulses can be corrected by this equation:

$$\frac{1}{T_1} = \frac{1}{T_1^*} + \frac{\ln(\cos(\theta))}{\tau} \quad (3)$$

In the above equation,  $T_1$  is the corrected  $T_1$ , while  $T_1^*$  is the measured  $T_1$ . The angle  $\theta$  is the small flip angle used to sample the magnetization over time and  $\tau$  is the time between samplings.

## Calculation for signal enhancement fold

The enhancement fold is derived as follows: the mass concentration of the MOF be denoted as  $c_1$ , and the signal intensity produced by the entrapped xenon in the MOF at this concentration be  $M_1$ . The signal per unit mass concentration of MOF is therefore  $M_1/c_1$ . For pure water,

let the mass concentration be  $c_2$ , and the signal intensity of the dissolved xenon in pure water be  $M_2$ . The signal per unit mass concentration of water is  $M_2/c_2$ . Thus, the enhancement fold, which compares the signal intensity per unit mass concentration of entrapped xenon in the MOF to the signal intensity per unit mass concentration of xenon in pure water, is calculated as:

$$\text{Enhancement fold} = \frac{M_1}{c_1} / \frac{M_2}{c_2} = \frac{M_1 * c_2}{M_2 * c_1} \quad (4)$$

### Xenon adsorption analysis and isosteric heat of adsorption

Xenon adsorption/desorption isotherms were performed on a Micromeritics 3 Flex automatic volumetric instrument. Before the isotherm measurement, NiZn-ZIF-8 and pristine ZIF-8 powders were degassed on 3 Flex for 10 h at 120 °C. The analysis temperature was kept at 273 and 298 K, respectively. Isosteric heat of adsorption ( $Q_{st}$ ) is used to evaluate the adsorption affinity of the gas molecules to the adsorbent material. Higher  $Q_{st}$  stands for stronger interactions between the adsorbate molecules and the adsorbent. The Clausius-Clapeyron equation was employed to calculate the  $Q_{st}$ :

$$Q_{st} = -RT^2 \left( \frac{\partial \ln P}{\partial T} \right)_{n_a} \quad (5)$$

Where  $n_a$  (mmol  $g^{-1}$ ) is the amount of adsorbed gas,  $T$  (K) is the temperature,  $P$  (kPa) is the pressure,  $Q_{st}$  (kJ  $mol^{-1}$ ) is the isosteric heat of adsorption.

### Molecular dynamics simulations

The initial structures for the MD simulations were constructed by three regions, namely as bath, MOF, and bath regions, which are segregated equally along the Z-axis. In the MOF region, the structures were adopted from the Cambridge Crystallographic Data Centre (CCDC No. 602542, <http://www.ccdc.cam.ac.uk>). The structure with a volume of  $34 \times 34 \times 34 \text{ \AA}^3$  is composed of  $2 \times 2 \times 2$  unit cells with the periodic structures in X-, Y-, and Z-axes. Terminal groups along in Z-axis were saturated by adding methyl ( $-\text{CH}_3$ ) groups. Each constructed structure was positioned at the center of the simulation box with dimensions  $34 \times 34 \times 102 \text{ \AA}^3$ , surrounded by 60 xenon atoms (Supplementary Fig. 85), using the Universal Force Field (UFF).

### Statistical analysis

Data are expressed as mean  $\pm$  standard deviation (SD) from at least three independent replicates. Statistical analysis was conducted using one-way analysis of variance (ANOVA), and two tailed Student's t-test was used for two-group comparisons, all performed within OriginPro 2021. Significance levels are indicated by asterisks: a  $p$ -value of less than 0.05 is the benchmark for statistical significance, \*\* for  $p < 0.01$ , and \*\*\* for  $p < 0.001$ .

### Data availability

The data that support the findings of this study, including the full image dataset, are available from the corresponding authors upon request. Source data are provided with this paper.

### References

- Zeng, Z., Liew, S. S., Wei, X. & Pu, K. Hemicyanine-based near-infrared activatable probes for imaging and diagnosis of diseases. *Angew. Chem. Int. Ed.* **60**, 26454 (2021).
- Wang, X. et al. Fluorescent probes for disease diagnosis. *Chem. Rev.* **124**, 7106–7164 (2024).
- Mugler, J. P. & Altes, T. A. Hyperpolarized  $^{129}\text{Xe}$  MRI of the human lung. *J. Magn. Reson. Imaging* **37**, 313–331 (2013).
- Li, H. et al. Damaged lung gas exchange function of discharged COVID-19 patients detected by hyperpolarized  $^{129}\text{Xe}$  MRI. *Sci. Adv.* **7**, eabc8180 (2021).
- Fang, Y. et al. Rapid pulmonary  $^{129}\text{Xe}$  ventilation MRI of discharged COVID-19 patients with Zigzag sampling. *Magn. Reson. Med.* **92**, 956–966 (2024).
- Rao, Q. et al. Assessment of pulmonary physiological changes caused by aging, cigarette smoking, and COPD with hyperpolarized  $^{129}\text{Xe}$  magnetic resonance. *Eur. Radiol.* **34**, 7450–7459 (2024).
- Zhou, Q. et al. Evaluation of injuries caused by coronavirus disease 2019 using multi-nuclei magnetic resonance imaging. *Magn. Reson. Lett.* **1**, 2–10 (2021).
- Doganay, O. et al. Time-series hyperpolarized xenon-129 MRI of lobar lung ventilation of COPD in comparison to V/Q-SPECT/CT and CT. *Eur. Radiol.* **29**, 4058–4067 (2019).
- Wang, J. M. et al. Using hyperpolarized  $^{129}\text{Xe}$  MRI to quantify regional gas transfer in idiopathic pulmonary fibrosis. *Thorax* **73**, 21–28 (2018).
- Rose, H. M. et al. Development of an antibody-based, modular biosensor for  $^{129}\text{Xe}$  NMR molecular imaging of cells at nanomolar concentrations. *Proc. Natl. Acad. Sci. USA* **111**, 11697–11702 (2014).
- Witte, C. et al. Live-cell MRI with xenon Hyper-CEST biosensors targeted to metabolically labeled cell-surface glycans. *Angew. Chem. Int. Ed.* **54**, 2806–2810 (2015).
- Klippel, S. et al. Cell tracking with caged xenon: using cryptophanes as MRI reporters upon cellular internalization. *Angew. Chem. Int. Ed.* **53**, 493–496 (2014).
- Wang, Y., Roose, B. W., Philbin, J. P., Doman, J. L. & Dmochowski, I. J. Programming a molecular relay for ultrasensitive biodetection through  $^{129}\text{Xe}$  NMR. *Angew. Chem. Int. Ed.* **55**, 1733–1736 (2016).
- Zhang, B. et al. An intracellular diamine oxidase triggered hyperpolarized  $^{129}\text{Xe}$  magnetic resonance biosensor. *Chem. Commun.* **54**, 13654–13657 (2018).
- Zhou, X., Graziani, D. & Pines, A. Hyperpolarized xenon NMR and MRI signal amplification by gas extraction. *Proc. Natl. Acad. Sci. USA* **106**, 16903–16906 (2009).
- Schröder, L., Lowery, T. J., Hilty, C., Wemmer, D. E. & Pines, A. Molecular imaging using a targeted magnetic resonance hyperpolarized biosensor. *Science* **314**, 446–449 (2006).
- Chen, Z. et al. Fine-tuning a robust metal-organic framework toward enhanced clean energy gas storage. *J. Am. Chem. Soc.* **143**, 18838–18843 (2021).
- Smoljan, C. S. et al. Engineering metal-organic frameworks for selective separation of hexane isomers using 3-dimensional linkers. *J. Am. Chem. Soc.* **145**, 6434–6441 (2023).
- Liu, Y. et al. Remarkably enhanced gas separation by partial self-conversion of a laminated membrane to metal-organic frameworks. *Angew. Chem. Int. Ed.* **54**, 3028–3032 (2015).
- Huang, J. et al. A microporous hydrogen-bonded organic framework based on hydrogen-bonding tetramers for efficient Xe/Kr separation. *Angew. Chem. Int. Ed.* **62**, e202315987 (2023).
- Jiang, J., Furukawa, H., Zhang, Y.-B. & Yaghi, O. M. High methane storage working capacity in metal-organic frameworks with acrylate links. *J. Am. Chem. Soc.* **138**, 10244–10251 (2016).
- Wang, H. et al. Docking of Cu(I) and Ag(I) in metal-organic frameworks for adsorption and separation of xenon. *Angew. Chem. Int. Ed.* **60**, 3417–3421 (2021).
- Banerjee, D. et al. Potential of Metal-organic frameworks for separation of xenon and krypton. *Acc. Chem. Res.* **48**, 211–219 (2015).
- Deng, H. et al. Multiple functional groups of varying ratios in metal-organic frameworks. *Science* **327**, 846–850 (2010).

25. Dong, Z., Sun, Y., Chu, J., Zhang, X. & Deng, H. Multivariate metal–organic frameworks for dialing-in the binding and programming the release of drug molecules. *J. Am. Chem. Soc.* **139**, 14209–14216 (2017).
26. Zhang, Z., Hanikel, N., Lyu, H. & Yaghi, O. M. Broadly tunable atmospheric water harvesting in multivariate metal–organic frameworks. *J. Am. Chem. Soc.* **144**, 22669–22675 (2022).
27. Fan, W. et al. Optimizing multivariate metal-organic frameworks for efficient C<sub>2</sub>H<sub>2</sub>/CO<sub>2</sub> separation. *J. Am. Chem. Soc.* **142**, 8728–8737 (2020).
28. Zhang, Y. et al. Introduction of functionality, selection of topology, and enhancement of gas adsorption in multivariate metal-organic framework-177. *J. Am. Chem. Soc.* **137**, 2641–2650 (2015).
29. Fan, W. et al. Multivariate polycrystalline metal-organic framework membranes for CO<sub>2</sub>/CH<sub>4</sub> separation. *J. Am. Chem. Soc.* **143**, 17716–17723 (2021).
30. Chen, C.-X. et al. Enhancing photocatalytic hydrogen production via the construction of robust multivariate Ti-MOF/COF composites. *Angew. Chem. Int. Ed.* **61**, e202114071 (2022).
31. Wang, Y. et al. A tunable multivariate metal-organic framework as a platform for designing photocatalysts. *J. Am. Chem. Soc.* **143**, 6333–6338 (2021).
32. Deliere, L. et al. Role of silver nanoparticles in enhanced xenon adsorption using silver-loaded zeolites. *J. Phys. Chem. C* **118**, 25032–25040 (2014).
33. Daniel, C. et al. Xenon capture on silver-loaded zeolites: characterization of very strong adsorption sites. *J. Phys. Chem. C* **117**, 15122–15129 (2013).
34. Bachetzky, C. et al. Adsorption of xenon, krypton, and their mixture on the flexible metal–organic framework DUT-8(Ni). *J. Phys. Chem. C* **128**, 6997–7006 (2024).
35. Xiong, S. et al. A microporous metal–organic framework with commensurate adsorption and highly selective separation of xenon. *J. Mater. Chem. A* **6**, 4752–4758 (2018).
36. Zeng, D. et al. Metal–organic frameworks possessing suitable pores for Xe/Kr separation. *Inorg. Chem.* **63**, 5151–5157 (2024).
37. Zeng, Q. et al. Hyperpolarized Xe NMR signal advancement by metal-organic framework entrapment in aqueous solution. *Proc. Natl. Acad. Sci. USA* **117**, 17558–17563 (2020).
38. Yang, Y. et al. Coloring ultrasensitive MRI with tunable metal-organic frameworks. *Chem. Sci.* **12**, 4300–4308 (2021).
39. Spence, M. M. et al. Functionalized xenon as a biosensor. *Proc. Natl. Acad. Sci. USA* **98**, 10654–10657 (2001).
40. Kunth, M., Witte, C., Hennig, A. & Schröder, L. Identification, classification, and signal amplification capabilities of high-turnover gas binding hosts in ultra-sensitive NMR. *Chem. Sci.* **6**, 6069–6075 (2015).
41. Li, R. et al. Nickel-substituted zeolitic imidazolate frameworks for time-resolved alcohol sensing and photocatalysis under visible light. *J. Mater. Chem. A* **2**, 5724–5729 (2014).
42. Stevens, T. K., Ramirez, R. M. & Pines, A. Nanoemulsion contrast agents with sub-picomolar sensitivity for xenon NMR. *J. Am. Chem. Soc.* **135**, 9576–9579 (2013).
43. Shapiro, M. G. et al. Genetically encoded reporters for hyperpolarized xenon magnetic resonance imaging. *Nat. Chem.* **6**, 630–635 (2014).
44. Zeng, Q. et al. Mitochondria targeted and intracellular biothiol triggered hyperpolarized <sup>129</sup>Xe magnetofluorescent biosensor. *Anal. Chem.* **89**, 2288–2295 (2017).
45. Wang, Y. & Dmochowski, I. J. Cucurbit[6]uril is an ultrasensitive Xe-129 NMR contrast agent. *Chem. Commun.* **51**, 8982–8985 (2015).
46. Zeng, Q. et al. Ultrasensitive molecular building block for biothiol NMR detection at picomolar concentrations. *iScience* **24**, 103515 (2021).
47. Schilling, F. et al. MRI thermometry based on encapsulated hyperpolarized xenon. *ChemPhysChem* **11**, 3529–3533 (2010).
48. Roukala, J. et al. Encapsulation of xenon by a self-assembled Fe<sub>4</sub>L<sub>6</sub> metallosupramolecular cage. *J. Am. Chem. Soc.* **137**, 2464–2467 (2015).
49. Du, K., Zemerov, S. D., Parra, S. H., Kikkawa, J. M. & Dmochowski, I. J. Paramagnetic organocobalt capsule revealing xenon host–guest chemistry. *Inorg. Chem.* **59**, 13831–13844 (2020).
50. Du, K., Zemerov, S. D., Carroll, P. J. & Dmochowski, I. J. Paramagnetic shifts and guest exchange kinetics in Co<sub>n</sub>Fe<sub>4–n</sub> metal–organic capsules. *Inorg. Chem.* **59**, 12758–12767 (2020).
51. Jayapaul, J. et al. Hyper-CEST NMR of metal organic polyhedral cages reveals hidden diastereomers with diverse guest exchange kinetics. *Nat. Commun.* **13**, 1708 (2022).
52. Tallavaara, P. & Jokisaari, J. 2D <sup>129</sup>Xe EXSY of xenon atoms in a thermotropic liquid crystal confined to a controlled-pore glass. *Phys. Chem. Chem. Phys.* **8**, 4902–4907 (2006).

## Acknowledgements

This work is supported by the Strategic Priority Research Program, CAS (XDB0540000), National Natural Science Foundation of China (82127802, 82441015), Key Research Program of Frontier Sciences, CAS (ZDBS-LY-JSC004), Hubei Provincial Key Technology Foundation of China (2021ACA013), Major Program (JD) of Hubei Province (2023BAA021), National Key Research and Development Program of China (2022YFC2410000), Hubei Provincial Natural Science Foundation of China (2022CFA050). Q.G. and L.S.B. acknowledge the support from the CAS Youth Interdisciplinary Team (JCTD-2022-13). Q.Z. acknowledges the support from the Youth Innovation Promotion Association, CAS (2023347), WUHAN TALENT, and the Hubei Provincial Natural Science Foundation of China (2023AFB790). Y. Yang acknowledges the support from the National Natural Science Foundation of China (22274162).

## Author contributions

X. Zhou, Q.G. and Q.Z. conceived the research. Q.G. and Q.Z. designed the experiments. Q.Z., Q.Y., M.Z., R.Z., Z.W., Z. X., Y. Yuan, and X. Zhao performed all the experiments. Q.Z., W.J., Y. Yang, and H.L. analyzed the data. Q.Z. wrote the original manuscript. Q.G., L.Z., X. Zhou, M.Y., and L.-S.B. edited the paper. Q.Z. and Q.Y. contributed equally to this work. All authors discussed the results and commented on the paper.

## Competing interests

The authors declare no competing interests.

## Additional information

**Supplementary information** The online version contains supplementary material available at <https://doi.org/10.1038/s41467-025-62110-4>.

**Correspondence** and requests for materials should be addressed to Qianni Guo or Xin Zhou.

**Peer review information** *Nature Communications* thanks Ivan Dmochowski who co-reviewed with Yannan Linand the other anonymous reviewer(s) for their contribution to the peer review of this work. A peer review file is available.

**Reprints and permissions information** is available at <http://www.nature.com/reprints>

**Publisher's note** Springer Nature remains neutral with regard to jurisdictional claims in published maps and institutional affiliations.

**Open Access** This article is licensed under a Creative Commons Attribution-NonCommercial-NoDerivatives 4.0 International License, which permits any non-commercial use, sharing, distribution and reproduction in any medium or format, as long as you give appropriate credit to the original author(s) and the source, provide a link to the Creative Commons licence, and indicate if you modified the licensed material. You do not have permission under this licence to share adapted material derived from this article or parts of it. The images or other third party material in this article are included in the article's Creative Commons licence, unless indicated otherwise in a credit line to the material. If material is not included in the article's Creative Commons licence and your intended use is not permitted by statutory regulation or exceeds the permitted use, you will need to obtain permission directly from the copyright holder. To view a copy of this licence, visit <http://creativecommons.org/licenses/by-nc-nd/4.0/>.

© The Author(s) 2025